

## Linear modeling of infragravity waves during Delilah

A. J. H. M. Reniers,<sup>1,3</sup> A. R. van Dongeren,<sup>1,4</sup> J. A. Battjes,<sup>1</sup> and E. B. Thornton<sup>2</sup>

Received 5 August 2001; revised 14 March 2002; accepted 17 April 2002; published 1 October 2002.

[1] The generation of infragravity waves by directionally spread shortwaves incident on an alongshore uniform beach is investigated. Two mechanisms responsible for the generation of infragravity waves are considered: the release of the bound infragravity waves associated with changes in the spatial variation of the incident shortwave energy and the forcing of trapped waves by obliquely incident directionally spread shortwaves. The infragravity wave response is examined using linear shallow water equations, taking into account the presence of bottom friction, setup of the mean water level, rollers, and longshore current. Summing all infragravity contributions due to difference interactions between pairs of shortwave spectral components with the same frequency difference results in infragravity energy density spectra. Calculated spectra are compared with measured spectra obtained during the Delilah field experiment for 11 consecutive days, including calm, mild, and storm conditions. In the comparison, attention is focused on the frequency distribution of the infragravity energy density throughout the surf zone and the transformation of the root mean square infragravity wave height. The measured infragravity response in the frequency range from 0.01 to 0.06 Hz is reproduced by the computations, with relatively broad spectra offshore and a clear nodal structure closer to shore. Typically 80% of the infragravity wave height variability is explained by the model of which 30% or less is due to bound infragravity waves. Differences occur mainly during storm events in which the infragravity energy is underpredicted in the outer surf zone and overpredicted in the inner surf zone. *INDEX TERMS:* 4255 Oceanography: General: Numerical modeling; 4546 Oceanography: Physical: Nearshore processes; 4560 Oceanography: Physical: Surface waves and tides (1255); *KEYWORDS:* infragravity waves, directional spreading, linear modeling, field data, surf zone dynamics

**Citation:** Reniers, A. J. H. M., A. R. van Dongeren, J. A. Battjes, and E. B. Thornton, Linear modeling of infragravity waves during Delilah, *J. Geophys. Res.*, 107(C10), 3137, doi:10.1029/2001JC001083, 2002.

### 1. Introduction

[2] The first observations that the temporal variation of incident shortwave heights (groups of higher waves) on the timescale of several minutes is responsible for the presence of infragravity waves in the nearshore were made by *Munk* [1949] (who introduced the term surfbeat to describe the phenomenon) and *Tucker* [1950]. They both observed a negative time lag between wave groups and surfbeat corresponding to wave groups travelling to shore and free infragravity waves returning. In addition, *Tucker* found a (smaller) negative correlation at zero time lag. *Longuet-Higgins and Stewart* [1962, 1964] suggested that bound infragravity waves, forced by the spatial changes of

momentum flux associated with normally incident shortwave groups, were somehow released in the surf zone returning as free infragravity waves after reflection at the shoreline. The bound infragravity waves propagate at the group velocity of the grouped shortwaves and are 180° out of phase with the shortwave envelope [*Biesel*, 1952], hence the negative correlation at zero time lag. *Longuet-Higgins and Stewart* [1962] indicated that if bed-slope effects can be neglected, the shoaling for the bound infragravity wave height is expected to be much stronger with depth ( $h^{-5/2}$ ) than that for the leaky free infragravity waves returning ( $h^{-1/4}$ ), which would explain the (greater) positive correlation at the negative time lag observed by *Munk* and *Tucker*.

[3] In the case of obliquely incident grouped shortwaves, free infragravity waves refract more strongly than bound infragravity waves (which follow the group). The outgoing infragravity waves may even be refractively trapped to the shoreline if the angle of incidence of the shortwave group is large enough. *Gallagher* [1971] showed that the nonlinear interaction between the shortwave groups and the trapped infragravity waves could lead to resonance where energy is transferred from the shortwaves to a class of trapped infragravity waves known as edge waves.

<sup>1</sup>Dutch Center for Coastal Research (NCK), Faculty of Civil Engineering and Geosciences, Delft University of Technology, Delft, Netherlands.

<sup>2</sup>Oceanography Department, Naval Postgraduate School, Monterey, California, USA.

<sup>3</sup>Presently at Oceanography Department, Naval Postgraduate School, Monterey, California, USA.

<sup>4</sup>Presently at Delft Hydraulics, P.O. Box 177, 2600 MH Delft, Netherlands.

[4] Yet another mechanism for the generation of infragravity waves was formulated by *Symonds et al.* [1982] who considered the temporal variation of the breakpoint position as a wave maker, generating infragravity waves propagating both offshore and onshore within the surf zone. The latter are reflected at the shoreline joining the free outgoing infragravity waves. Alternatively the breakpoint is fixed, allowing for infragravity wave generation in the inner surf zone [*Foda and Mei*, 1981; *Schäffer and Svendsen*, 1988; *Watson and Peregrine*, 1992].

[5] Measurements of surf zone elevation spectra [e.g., *Suhayda*, 1974; *Huntley*, 1976; *Holman*, 1981] have shown the importance of infragravity energy with a clear dominance close to the shore line [*Huntley et al.*, 1981; *Thornton and Guza*, 1982]. Outside the surf zone (at 13 m on the Atlantic coast), *Elgar et al.* [1992] used bispectral analysis [*Hasselmann et al.*, 1963] to show that the contribution of the bound infragravity waves to the total infragravity spectrum increased with more energetic short-wave conditions. The bound infragravity contribution did not exceed 50% and was typically much less for the predominant moderate conditions. At shallower depths the contribution of bound infragravity waves can increase further [*Elgar et al.*, 1992; *Ruessink*, 1998]. Directional analysis by *Herbers et al.* [1995a] showed that infragravity waves have a much broader distribution, propagating both up-coast and down-coast, than the incident shortwaves. This analysis also showed that refractive trapping of infragravity waves is stronger for directionally broad shortwaves, which is expected to result in cross-shore infragravity wave height variations proportional to  $h^{-1/2}$  as opposed to the leaky waves considered by *Longuet-Higgins and Stewart* [1962]. The presence of a strong longshore surf zone current is also known to have an effect on infragravity waves. The latter was assessed by *Howd et al.* [1992], showing a change in the edge wave dispersion curves and the cross-shore structure due to the presence of a strong longshore current.

[6] Infragravity motions in the nearshore forced by normally incident shortwave groups have been studied using both time domain models [*List*, 1992; *Roelvink*, 1993; *Watson and Peregrine*, 1992] and spectral modeling [*van Leeuwen*, 1992]. The possibility of infragravity forcing by obliquely incident grouped shortwaves on an alongshore uniform beach was incorporated in an analytical model by *Schäffer* [1993, 1994], assessing the generation of both leaky waves and trapped waves. Directional spreading in the wave group forcing is generally not taken into account in these models, though this can be of significant importance [*Herbers et al.*, 1995b]. *Gallagher* [1971] did consider directional spreading but used rather crude assumptions to model the processes within the surf zone. *Okiihiro et al.* [1992] used *Hasselmann's* [1962] theory to predict the bound infragravity energy for directionally spread shortwaves at 8 and 13 m water depth explaining at most 50% of the total infragravity energy present, and usually much less (in line with the observations by *Elgar et al.* [1992]). *Herbers et al.* [1994], utilizing more accurate measurements of directionally spread shortwaves, obtained good agreements between the measured and predicted bound infragravity wave spectra. *Herbers et al.* [1995b] used the theory by *Hasselmann*

[1962] and a WKB expansion in combination with the theory of *Longuet-Higgins and Stewart* [1962] to predict the propagation properties of directionally spread low-frequency energy density outside the surf zone (at 13 m water depth) and found good agreement with the measured ratios of up-coast and down-coast propagating infragravity energy fluxes.

[7] The potential importance of infragravity waves is linked to the observation that spatial scales of morphological surf zone features correspond to length scales of infragravity waves and more specifically edge waves [*Bowen and Inman*, 1971; *Holman and Bowen*, 1982]. The relative importance of sediment transport induced by infragravity waves in relation to other transport mechanisms in the surf zone was investigated by *Roelvink and Stive* [1989] and *Roelvink* [1993], showing it to be a significant contribution to the total cross-shore sediment transport.

[8] In the following, the generation of infragravity waves by directionally spread incident shortwaves on an alongshore uniform beach is considered. The following mechanisms responsible for the generation of infragravity waves are incorporated: the release of the bound infragravity waves associated with changes in the spatial variation of the incident shortwave energy [*Longuet-Higgins and Stewart*, 1962, 1964], the interaction between the directionally spread shortwaves and trapped waves [*Gallagher*, 1971] and the shortwave energy modulation within the surf zone [*Foda and Mei*, 1981; *Schäffer and Svendsen*, 1988; *Watson and Peregrine*, 1992]. These mechanisms are examined using linear shallow water equations. The equations are solved in the frequency domain, assuming stationary (wind-wave and infragravity) conditions. This implies that the growth (decay) time-scales of the infragravity waves are relatively short with respect to the measuring time interval. *Lippmann et al.* [1997] estimated the half-life decay timescale to be of the order of 10–30 edge wave periods, which is less than the approximately 2 hour measurement period for the infragravity spectra considered here [ $0.01 \text{ Hz} < f < 0.06 \text{ Hz}$ ]. The model can be used to predict the infragravity energy generated by directionally spread shortwaves on an arbitrary bottom profile. Bottom friction is introduced to prevent the unbounded growth in the case of edge wave resonance.

[9] The reasons to use linearized equations are twofold. First, it gives the possibility to examine the various infragravity wave generation mechanisms in their basic form (without nonlinear interactions complicating the analysis). Second, it gives a quick assessment (computational time is an order of magnitude smaller) of the conditions which are interesting, and thus can provide the necessary selection for the more complex nonlinear modeling (*A. R. van Dongeren et al.*, Nonlinear modelling of infragravity wave response during Delilah, submitted to *Journal of Geophysical Research*, 2002).

[10] To verify the model behavior, a comparison is made with the measurement data obtained during the Delilah field experiment [*Birkemeier et al.*, 1997] in Duck, North Carolina. Pressure data transformed to surface elevation are analyzed to obtain the transformation of infragravity energy throughout the surf zone for various shortwave

conditions. An assessment of the infragravity motions within these data was performed earlier by *Lippmann et al.* [1998]. In the present comparison, the attention is focused on low-frequency surface elevation spectra and the corresponding low-frequency root mean square wave height.

## 2. Model Equations

### 2.1. Introduction

[11] We consider a spectrum of short waves narrow in both frequency and direction, incident on a beach uniform in the alongshore direction with arbitrary cross-shore bottom profile. Two types of motions are considered: those that occur on the timescale of many wave groups and are essentially considered “steady,” such as the mean wave height transformation, the setup of the mean water level and the mean longshore current, and those that occur on the timescale of wave groups, i.e., the generation of infragravity waves, being typically in the order of 20 s to a few minutes in the field.

[12] The equations to model the mean motions are similar to the ones used by *Reniers and Battjes* [1997] (referred to as RB97 hereafter) and are not reported here. The mean wave transformation and corresponding setup of the mean water level are computed using the roller concept. The measured root mean square shortwave height is used to calibrate the model coefficients for the mean wave energy dissipation. This results in a computed cross-shore distribution of wave energy and setup of the mean water level, both of which are used in modeling the generation of infragravity waves.

### 2.2. Infragravity Equations

[13] In this section motions that occur on the timescale of wave groups are considered. To obtain the appropriate equations, the relevant variables are averaged over the incident shortwave period with the means subtracted. Linearizing the shallow water equations as given by *Phillips* [1977], the slowly varying continuity equation is given by:

$$\frac{\partial \eta}{\partial t} + \frac{\partial(hu)}{\partial x} + \frac{\partial(hv)}{\partial y} = 0 \quad (1)$$

where  $x$  is positive onshore and  $y$  directed alongshore using the Cartesian convention,  $\eta$  is the long wave surface elevation,  $u$  and  $v$  the corresponding cross-shore and alongshore velocities and  $h$  the total water depth including the mean setup. The cross-shore momentum balance reduces to:

$$\rho h \frac{\partial u}{\partial t} + \rho g h \frac{\partial \eta}{\partial x} = -\frac{\partial S_{xx}}{\partial x} - \frac{\partial S_{xy}}{\partial y} \quad (2)$$

and the alongshore momentum equation:

$$\rho h \frac{\partial v}{\partial t} + \rho g h \frac{\partial \eta}{\partial y} = -\frac{\partial S_{yy}}{\partial y} - \frac{\partial S_{yx}}{\partial x} \quad (3)$$

where  $S_{ij}$  represents the shortwave radiation stresses [Longuet-Higgins and Stewart, 1964] varying at the wave groupscale forcing the infragravity waves. Combining

these equations results in a single equation for the infragravity wave surface elevation [*Mei and Benmoussa*, 1984]:

$$\begin{aligned} & -\frac{1}{g} \frac{\partial^2 \eta}{\partial t^2} - \frac{\mu}{g} \frac{\partial \eta}{\partial t} + h \frac{\partial^2 \eta}{\partial x^2} + \frac{dh}{dx} \frac{\partial \eta}{\partial x} + h \frac{\partial^2 \eta}{\partial y^2} \\ & = \frac{-1}{\rho g} \left( \frac{\partial^2 S_{xx}}{\partial x^2} + \frac{2\partial^2 S_{yx}}{\partial x \partial y} + \frac{\partial^2 S_{yy}}{\partial y^2} \right) \end{aligned} \quad (4)$$

to which a linear damping term with resistance factor  $\mu$  has been added [*Gallagher*, 1971]. The forcing on the right hand side of the long wave equation is determined by the frequency-directional spectrum of the shortwaves. Considering the full shortwave spectrum, a bound infragravity wave will be forced at the difference frequency of each combination of two spectral components. Since this equation is linear, the contribution of each pair of spectral components to the infragravity surface elevation can be computed independently, and then integrated to yield the total infragravity surface elevation. Starting with a combination of two shortwave spectral components of different frequencies,  $f_i$ , with corresponding wave numbers  $k_i$  and arbitrary shoreward directions  $\alpha_i$ , the slowly modulating radiation stress made up by these two components is described by [*Schäffer*, 1993]:

$$\begin{aligned} & S_{xx}(x, y, t, f_1, f_2, k_{y,1}, k_{y,2}) \\ & = \frac{1}{2} \hat{S}_{xx}(x, f_1, f_2, k_{y,1}, k_{y,2}) \exp[i(2\pi \Delta f t - \Delta k_y y)] + * \end{aligned} \quad (5)$$

$$\begin{aligned} & S_{xy}(x, y, t, f_1, f_2, k_{y,1}, k_{y,2}) \\ & = \frac{1}{2} \hat{S}_{xy}(x, f_1, f_2, k_{y,1}, k_{y,2}) \exp[i(2\pi \Delta f t - \Delta k_y y)] + * \end{aligned} \quad (6)$$

$$\begin{aligned} & S_{yy}(x, y, t, f_1, f_2, k_{y,1}, k_{y,2}) \\ & = \frac{1}{2} \hat{S}_{yy}(x, f_1, f_2, k_{y,1}, k_{y,2}) \exp[i(2\pi \Delta f t - \Delta k_y y)] + * \end{aligned} \quad (7)$$

where \* stands for the complex conjugate and the infragravity frequency is obtained from the frequency difference:

$$\Delta f = f_1 - f_2 \quad (8)$$

with the corresponding alongshore wave number:

$$\Delta k_y = k_{y,1} - k_{y,2} = k_1 \sin \alpha_1 - k_2 \sin \alpha_2 \quad (9)$$

and cross-shore wave number:

$$\Delta k_x = k_{x,1} - k_{x,2} = k_1 \cos \alpha_1 - k_2 \cos \alpha_2 \quad (10)$$

Given the alongshore uniformity of the beach, the radiation stress modulation is periodic in both time and alongshore direction whereas the cross-shore variation is given by the complex amplitude of the radiation stress modulation (temporarily dropping the dependencies):

$$\hat{S}_{xx} = \left( \left( n(1 + \cos^2 \hat{\alpha}) - \frac{1}{2} \right) \hat{E}_w + 2 \cos^2 \hat{\alpha} \hat{E}_r \right) \exp \left[ -i \int \Delta k_x dx \right] \quad (11)$$

$$\hat{S}_{xy} = \left( n \cos \hat{\alpha} \sin \hat{\alpha} \hat{E}_w + 2 \cos \hat{\alpha} \sin \hat{\alpha} \hat{E}_r \right) \cdot \exp \left[ -i \int \Delta k_x dx \right] \quad (12)$$

$$\hat{S}_{yy} = \left( \left( n(1 + \sin^2 \hat{\alpha}) - \frac{1}{2} \right) \hat{E}_w + 2 \sin^2 \hat{\alpha} \hat{E}_r \right) \exp \left[ -i \int \Delta k_x dx \right] \quad (13)$$

where  $n$  is the ratio of group velocity over phase velocity,  $\hat{E}_w$  and  $\hat{E}_r$  are the wave and roller energy modulation amplitudes, to be obtained from a wave and roller energy balance respectively, and  $\hat{\alpha}$  is the mean incidence angle of the two spectral components:

$$\hat{\alpha} = \text{atan} \left( \frac{k_{y,1} + k_{y,2}}{k_{x,1} + k_{x,2}} \right) \quad (14)$$

The individual wave angles,  $\alpha_i$  are obtained with Snell's law and the corresponding wave numbers are obtained from the linear dispersion relation. Infragravity wave solutions that are also periodic in both time and alongshore direction are found as [Eckart, 1951]:

$$\begin{aligned} \eta(x, y, t, f_1, f_2, k_{y,1}, k_{y,2}) \\ = \frac{1}{2} \hat{\eta}(x, f_1, f_2, k_{y,1}, k_{y,2}) \exp [i(2\pi \Delta f t - \Delta k_y y)] + * \end{aligned} \quad (15)$$

where the complex amplitude  $\hat{\eta}$  varies in the cross-shore only. Introducing equation (15) together with equations (5)–(7) into the infragravity surface elevation equation (4) results in an ordinary second-order differential equation (dropping the temporal and alongshore periodicity):

$$\begin{aligned} \left( h \frac{d^2 \hat{\eta}}{dx^2} + \frac{dh}{dx} \frac{d\hat{\eta}}{dx} + \left( \frac{4\pi^2 \Delta f^2}{g} - \frac{i\mu 2\pi \Delta f}{g} - h \Delta k_y^2 \right) \hat{\eta} \right) \\ = \frac{1}{\rho g} \left( \frac{d^2 \hat{S}_{xx}}{dx^2} - 2i \Delta k_y \frac{d\hat{S}_{yx}}{dx} + \Delta k_y^2 \hat{S}_{yy} \right) \end{aligned} \quad (16)$$

The radiation stress gradients are calculated from the cross-shore distribution of the wave and roller energy modulation amplitudes associated with the two spectral components. The wave energy modulation amplitude is obtained from a wave energy balance:

$$\frac{d\hat{E}_w(x, f_1, f_2, k_{y,1}, k_{y,2})}{dx} c_g \cos(\hat{\alpha}) = -\hat{D}_w(x, f_1, f_2, k_{y,1}, k_{y,2}) \quad (17)$$

where  $\hat{D}_w$  is the dissipation of the energy modulation and  $c_g$  represents the group velocity at the peak frequency of the shortwave spectrum (assumed to be narrow) obtained with linear theory. The dissipation of the energy modulation determines the generation of infragravity waves in the surf zone, and is defined as a linear proportion of the total

mean wave energy dissipation  $\bar{D}_w$  [Eldeberky and Battjes, 1996]:

$$\hat{D}_w(x, f_1, f_2, k_{y,1}, k_{y,2}) = \frac{\hat{E}_w(x, f_1, f_2, k_{y,1}, k_{y,2})}{\bar{E}_w} \bar{D}_w \quad (18)$$

(the over bar indicates averaging over many wave groups) allowing the groupiness to enter the surf zone, but still taking into account the randomness of the wave field (versus a fixed breakpoint position). Both  $\bar{D}_w$  and  $\bar{E}_w$  are obtained from the mean wave energy balance (following RB97). The boundary condition for the modulated wave energy balance (equation (17)) is obtained from the individual spectral densities,  $S_0(f_i, \alpha_i)$ , at the offshore boundary (denoted by the subscript 0):

$$\hat{E}_{w,0} = \rho g [S_0(f_1, \alpha_1) S_0(f_2, \alpha_2)]^{\frac{1}{2}} \delta f \delta \alpha \quad (19)$$

where  $\delta f$  represents the frequency resolution and  $\delta \alpha$  the directional resolution of the frequency-directional spectrum.

[14] The amplitude of the roller energy modulation is obtained from the roller energy balance given by [Nairn et al., 1990; Stive and de Vriend, 1994]:

$$\begin{aligned} 2 \frac{d\hat{E}_r(x, f_1, f_2, k_{y,1}, k_{y,2})}{dx} c \cos(\hat{\alpha}) \\ = \hat{D}_w(x, f_1, f_2, k_{y,1}, k_{y,2}) - \hat{D}_r(x, f_1, f_2, k_{y,1}, k_{y,2}) \end{aligned} \quad (20)$$

with  $c$  the wave celerity at the peak frequency of the shortwave spectrum. The modulated roller energy dissipation is described as a linear proportion of the mean roller dissipation,  $\bar{D}_r$ , obtained from the mean roller energy balance (RB97; equation (9)):

$$\hat{D}_r(x, f_1, f_2, k_{y,1}, k_{y,2}) = \frac{\hat{E}_w(x, f_1, f_2, k_{y,1}, k_{y,2})}{\bar{E}_w} \bar{D}_r \quad (21)$$

Once the cross-shore evolution of the wave and roller energy modulations are known, the radiation stress gradients due to the two spectral components can be computed and the forcing on the right hand side of equation (16) is known.

[15] The resistance factor in the left hand side of equation (16) is defined as:

$$\mu = \frac{c_f |U|}{h} \quad (22)$$

where  $c_f$  is a friction factor and the mean velocity is given by:

$$|U| = [U_{rms}^2 + V^2]^{\frac{1}{2}} \quad (23)$$

with  $U_{rms}$  as the computed root mean square shortwave near-bed velocity and  $V$  the measured mean longshore current velocity with a linear interpolation for the intermediate points.

[16] Besides damping by bottom friction, the presence of a strong longshore current is known to change both the edge

wave dispersion and the cross-shore structure of the edge waves [Howd *et al.*, 1992]. They found that the presence of a longshore current can be incorporated by defining an effective depth profile:

$$h' = \frac{h}{\left(1 - \frac{U}{c_y}\right)^2} \quad (24)$$

in which  $c_y$  is the alongshore infragravity wave celerity:

$$c_y = \frac{2\pi\Delta f}{\Delta k_y} \quad (25)$$

Using this effective depth, the second-order differential equation for the infragravity waves (equation (16)), with a small modification for the RHS (Appendix A), is numerically solved using central finite differences. The boundary conditions are given by a zero flux at the shore line and a free oblique outgoing (or trapped) infragravity wave combined with an incident bound infragravity wave offshore (Appendix B). The forced energy density for a specific low frequency,  $\Delta f$ , is obtained by integrating over the appropriate variables:

$$S(x, \Delta f) =$$

$$\int_{f_{c,lo}}^{\infty} \int_{-\infty}^{\infty} \int_{-\infty}^{\infty} \frac{1}{2} |\hat{\eta}(x, f + \Delta f, f, k_{y,1}, k_{y,2})|^2 dk_{y,1} dk_{y,2} df \quad (26)$$

where  $f_{c,lo}$  is a low-frequency cutoff set at 0.06 Hz defining the infragravity part of the frequency spectrum. The bound infragravity portion,  $S_b(x, \Delta f)$ , of the total infragravity energy density,  $S(x, \Delta f)$ , is obtained directly from the directionally spread shortwave spectrum (see Appendix C):

$$S_b(x, \Delta f) = 2 \int_{f_{c,lo}}^{\infty} \int_{-\frac{\pi}{2}}^{\frac{\pi}{2}} \int_{-\frac{\pi}{2}}^{\frac{\pi}{2}} |C|^2 S(f + \Delta f, \alpha_1) S(f, \alpha_2) df d\alpha_1 d\alpha_2 \quad (27)$$

where the difference interaction coefficient  $C$  is given by:

$$C(f + \Delta f, f, \alpha_1, \alpha_2) = \frac{g \left( n \left( 1 + \cos^2 \left( \hat{\alpha} - \hat{\theta}_{in} \right) \right) - \frac{1}{2} \right)}{\left( \frac{4\pi^2 \Delta f^2}{\Delta k^2} - \frac{i\pi 2\pi \Delta f}{\Delta k^2} - gh \right)} \quad (28)$$

The incidence angle of the bound infragravity wave is determined by the two spectral shortwave components forcing it:

$$\hat{\theta}_{in} = \text{atan} \left( \frac{k_{y,1} - k_{y,2}}{k_{x,1} - k_{x,2}} \right) \quad (29)$$

In the following, these computed spectral estimates are compared with measurements acquired during the Delilah field experiment [Birkemeier *et al.*, 1997].

### 3. Comparison With Measurements

#### 3.1. Mean Characteristics

[17] The Delilah experiment was performed in 1990 at the US Army Corps of Engineers Field Research Facility at

Duck, North Carolina. A plan view of the experimental layout is shown in Figure 1. Only the cross-shore array of colocated pressure transducers and velocity meters within the minigrd (Figure 1 and Table 1) is used in the comparison. The most inshore point, CM10, is subject to intermittent drying and flooding, which is not represented in the computations. This point has therefore been excluded from the model measurement comparisons.

[18] The frequency-directional spectra (Figure 2) obtained at the 8 m FRF array are used as boundary conditions for the modulated wave energy balance (equations (17) and (19)). These spectra are calculated from 2 hour and 16 min records using a Maximum Likelihood Estimator [Long and Atmadja, 1994] starting at 3 hour intervals. The same record length is used in computing the frequency spectra from the cross-shore array of pressure sensors. The record length is considered to be long enough to give a reliable estimate of the low-frequency spectrum and short enough to avoid nonstationarity in the shortwave forcing (e.g., due to the tide). The resulting shortwave frequency directional spectra utilized in the present computations have a frequency resolution of 0.01 Hz and a directional resolution of 5°.

[19] The comparison with measurements spans an 11 day period starting on 7 October. For each consecutive day the bottom profile nearest to the cross-shore array was used in the calculation. The profile was extended to the 8 m depth contour with a profile obtained from the larger bathymetric map (Figure 1) because the minigrd area extended only to approximately the 4 m water depth contour. The larger overall bathymetry was measured 1 month prior to the experiment, so errors in the actual bed level can be present. Still, the extension to 8 m depth is important in view of the generation of free long waves between the 8 m and 4 m depth contours. Extending the bottom profile to even deeper water showed negligible differences in the computed infragravity spectra, indicating that the generation of long waves by the incoming shortwaves beyond a water depth of 8 m can be ignored under the present circumstances. For severe storm conditions with high waves and corresponding long periods, for which shoaling and refraction are still of importance at 8 m water depth, the computational domain should be extended to deeper water.

[20] The mean wave energy balance (RB97; equation (1)) is initialized using the mean shortwave energy at 8 m water depth, obtained by integrating the FRF 8 m array frequency-directional shortwave spectrum:

$$\bar{E}_{w,0} = \rho g \int_{-\frac{\pi}{2}}^{\frac{\pi}{2}} \int_{f_{c,lo}}^{0.4\text{Hz}} S(f, \alpha) df d\alpha \quad (30)$$

considering the incident ( $-\pi/2 < \alpha < \pi/2$ ) shortwaves ( $f_{c,lo} > 0.06$  Hz) only. The mean shortwave energy is related to the shortwave root mean square wave height through:

$$H_{rms,hi} = \left( \frac{8\bar{E}_w}{\rho g} \right)^{\frac{1}{2}} \quad (31)$$

[21] Calculating  $H_{rms,hi}$  for 11 consecutive days results in a picture of the three hourly changes of the shortwave conditions at the offshore boundary. A synoptic view of the measured wave conditions along with mean water level

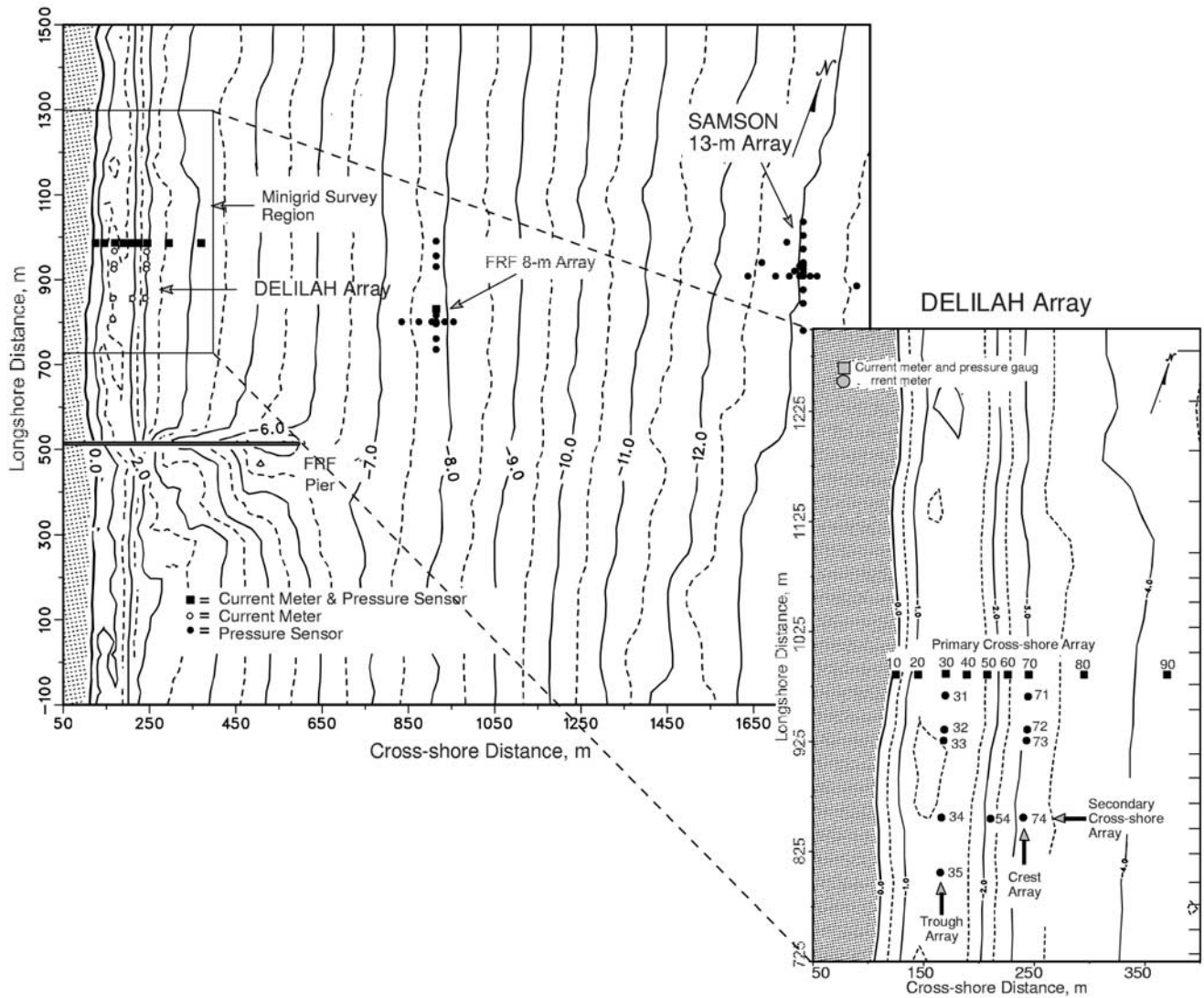


**Figure 1.** Bathymetry and instrument positions during the Delilah field experiment (Courtesy of Birkemeier et al. [1997, Figure 2]).

changes and maximum longshore current velocities are shown in Figure 3. Calm swell conditions from the southeast prevail during the first days, with  $H_{rms,hi}$  well below 0.5 m. On 8 October the wave height starts increasing, reaching moderate conditions at the beginning of 10 October, with  $H_{rms,hi}$  in the order of .7 m, followed by a storm during the following day. On 12 October the storm abates, followed by the arrival of another storm, still from the southeast at the end of the same day, with clearly more energy than the previous days, building up to  $H_{rms,hi}$  of 1.7 m at the beginning of 13 October. This storm abates in the next 2 days, followed by a small increase in wave height at the end of 14 October and later on a change in the mean wave direction on 16 October when local seas incident from the northeast dominated the shortwave spectrum. After 16 October the wave conditions become mild with typically quite broad spectral distributions in both frequency and direction. In correspondence with the predominant wave incidence from the southeast, the maximum longshore currents are mostly northward directed with longshore current velocities in excess of 1.5 m/s during the peak of

the storm on 11 October. The tidal variation is in the order of 1 m with an increased setup during the larger storm events.

[22] The cross-shore shortwave transformation is calibrated for each run with the measured  $H_{rms,hi}$  calculated from the 2 hour and 16 min cross-shore array pressure sensor records, to obtain the model coefficient  $\gamma$  (RB97; equation (4)) for the mean wave energy dissipation. This resulted in a mean  $\gamma$  value for the 11 day period of 0.45 with a standard deviation of 0.055.

[23] A typical example of the computed wave transformation compared with measurements on 10 October for hour 7 is shown in Figure 4. The significant wave height at that time was 1.14 m with a peak frequency of 0.103 Hz and a mean direction of approximately  $-40^\circ$  with respect to the

**Table 1.** Position of Combined Pressure and Velocity Sensors in the Cross-Shore Array Within the Minigrid Area

Current meter	20	30	40	50	60	70	80	90
X (m)	145	170	189	207	226	245	295	370

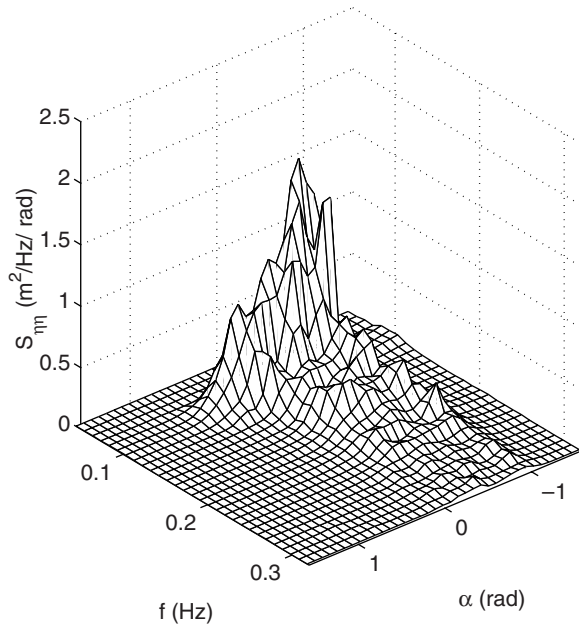


**Figure 2.** Frequency-directional spectrum at FRF 8 m array on 10 October for hour 7. Directions given with respect to the shore normal, positive from the northeasterly quadrant.

shore normal at the FRF 8 m array (i.e., waves incident from the southeast). Wave breaking occurs on the bar (which was present after 9 October) and near the shore line.

[24] Plotting the measured  $H_{rms,hi}$  versus the computed  $H_{rms,hi}$  for all model runs shows that errors in the computed wave heights are within 15% of the measured wave heights (Figure 5). The roller dissipation coefficient  $\beta$  is kept at a value of 0.05 for all conditions in correspondence with the results obtained by *Ruessink et al.* [2001]. The longshore current on 10 October for hour 7 has a maximum velocity of 1 m/s located in the trough, which is typical for the 11 day period considered here [Thornton and Kim, 1993]. The friction coefficient  $c_f$  is kept at a constant value of 0.007 in line with the longshore current computations of *Church and Thornton* [1993] utilizing a linear bottom friction.

### 3.2. Infragravity Characteristics

[25] The procedure to compare computational results for the infragravity waves with measurements is explained below in discussing the results for 10 October, hour 7. This procedure is then performed for each 3 hour interval within the period from 7 to 17 October. The frequency-directional spectrum for 10 October for hour 7 is shown in Figure 2 as an example.

[26] The measured low-frequency surface elevation spectra are calculated from the transformed 2 hour and 16 min

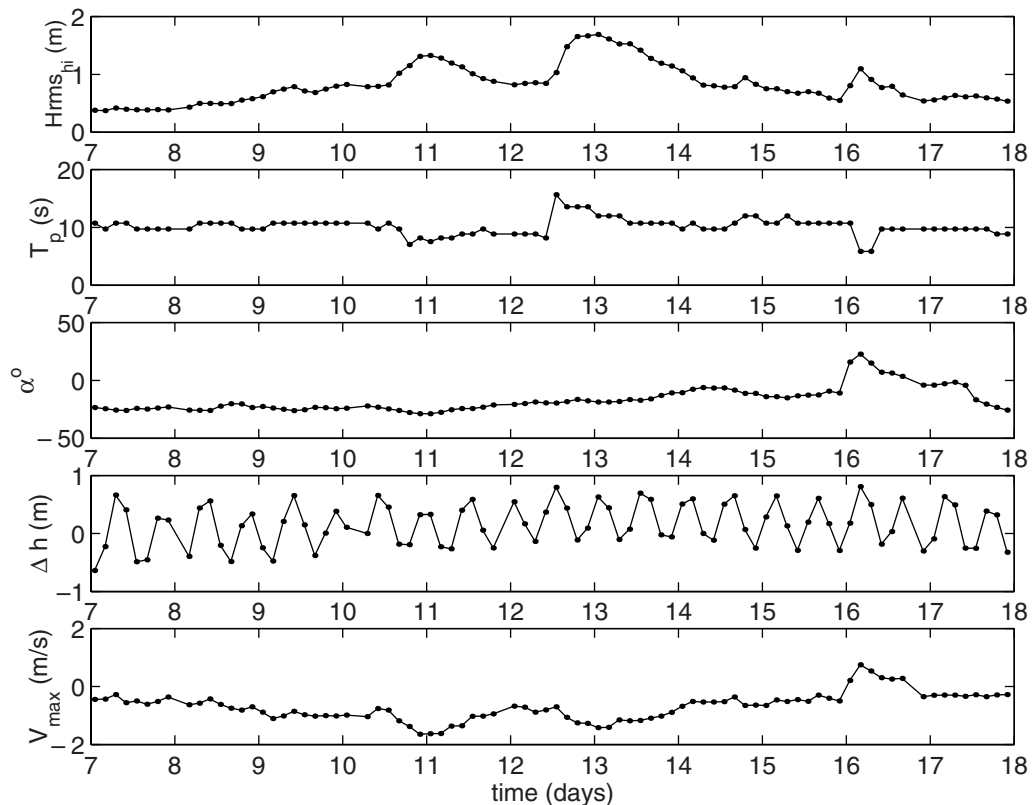


**Figure 3.** Mean wave/flow conditions for 7–18 October at 3 hour intervals indicated by the dots. Upper panel: Measured  $H_{rms,hi}$  at the FRF 8 m array. Upper middle panel: Corresponding peak period ( $T_p$ ). Middle panel: Mean angle of incidence at the FRF 8 m array. Lower middle panel: Tidal elevation. Lower panel: Maximum longshore current velocity within the surf zone.

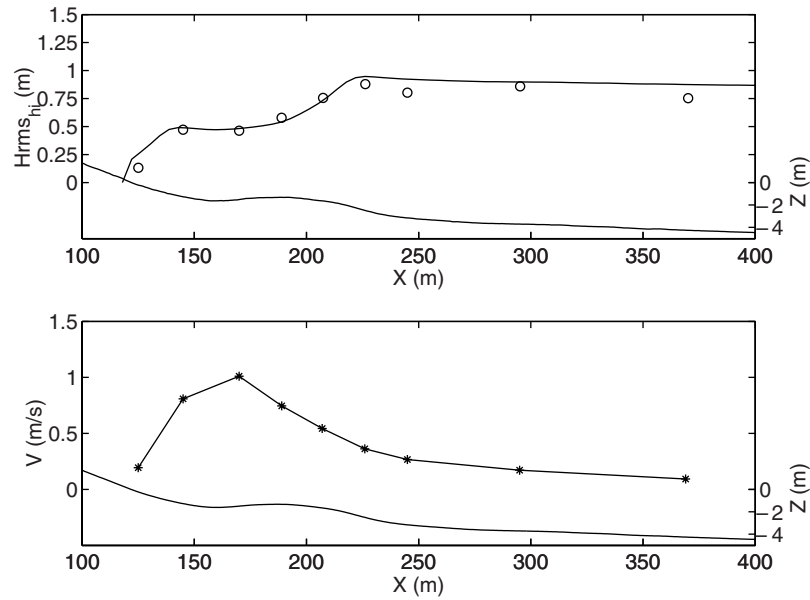


**Figure 4.** Upper panel: Computed (solid line) and measured (o) root mean square wave height on 10 October for hour 7. Bottom profile given as a reference. Lower panel: Corresponding measured longshore current velocity (\*).

pressure records with Hanning windowed subseries of 128 s resulting in a frequency resolution of 0.0078 Hz and 128 degrees of freedom. The measured forced/bound infragravity energy density is calculated using a bispectral analysis [Hasselmann *et al.*, 1963] on the same record.

[27] The computed (equations (27) and (28)) and measured bound infragravity energy density at CM90 match well (see Figure 6). Note that differences between measurements and computations may occur given that equation (27) does not take slope effects into account. This effect is expected to

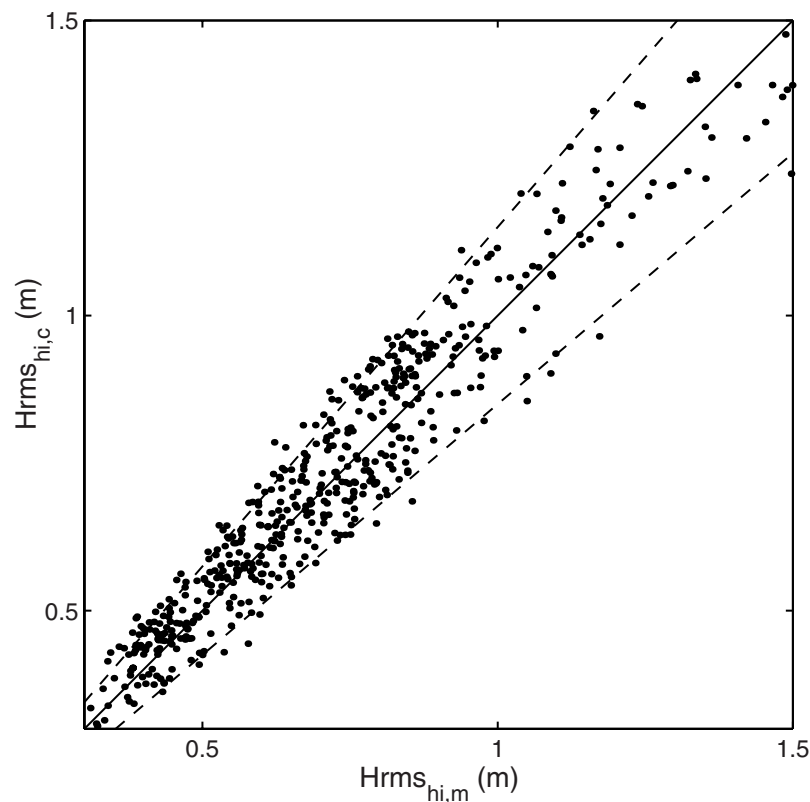


**Figure 5.** Computed (subscript c) versus measured (subscript m)  $H_{rms,hi}$  over the 11 day period considered, with 15% error bands indicated by the dashed lines.

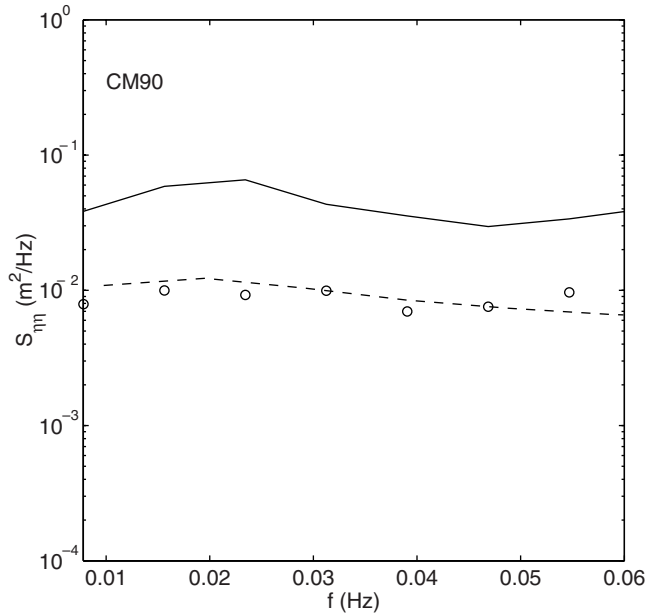


**Figure 6.** Measured total (solid line), computed bound (dashed line), and measured bound (o) infragravity surface elevation energy density at sensor location CM90 on 10 October for hour 7.

be small provided the local wave height over water depth ratio is relatively small. It is clear from Figure 6 that the free infragravity wave energy is substantially larger than the bound infragravity wave energy, which contributes approximately 20% to the total infragravity energy present.

[28] The computed and measured total infragravity energy densities for all instrument positions in the cross-shore array are compared in Figure 7. For most instrument positions the overall energy density levels are near the measured values though differences for specific frequencies can be significant (e.g., a factor of two for  $F = 0.03$  Hz at CM40). There is a consistent underestimation of the energy

density at 0.01 Hz. The computed and measured frequency distribution of the energy density is broad for the offshore measuring positions (viz. CM90–CM80), but becomes more structured as the measuring positions get closer to the shoreline (CM70–CM40), with clear nodal points close to the shore (CM30 and CM20).

[29] Integration of the energy density  $S(x, \Delta f)$  over the infragravity band (0.01–0.06 Hz) allows an estimate of the low-frequency root mean square wave height,  $H_{rms,lo}$  (defined similar to  $H_{rms,hi}$ ), which is compared with the measurements (Figure 8). Going shoreward through the surf zone, the  $H_{rms,lo}$  increases with decreasing water depth and then decreases in the trough. The general behavior is followed by the model, though the computed  $H_{rms,lo}$  increases less over the bar compared with the measurements. The observed shoaling offshore of the bar crest appears stronger than the theoretical shoaling associated with leaky waves ( $h^{-1/4}$  calibrated with the measured  $H_{rms,lo}$  at CM20), although the differences are small, which prevents a firm conclusion. The bound infragravity wave height is seen to increase toward the bar crest, though the contribution to the total infragravity wave height stays less than 50% throughout the surf zone. Once the waves start breaking over the bar (Figure 4), the bound infragravity wave height decreases accordingly. It is noted that although the bispectral analysis can be applied at an arbitrary depth, there is no longer a clear distinction between forced/bound and free infragravity waves at very shallow depths where  $c_g \sim \sqrt{gh}$ .

[30] Still, even at shallow water depths the bispectrum is expected to represent the phase coupling between the incident waves and infragravity waves and as such some measure of the bound infragravity waves [Ruessink, 1998], though the results should be interpreted with some caution.

[31] Next the infragravity energy is examined for the 11 day period. The comparison between the computed and measured frequency distribution of the infragravity energy density for CM90 is shown in the upper and middle panel of Figure 9. Energy density levels are low for the first few days

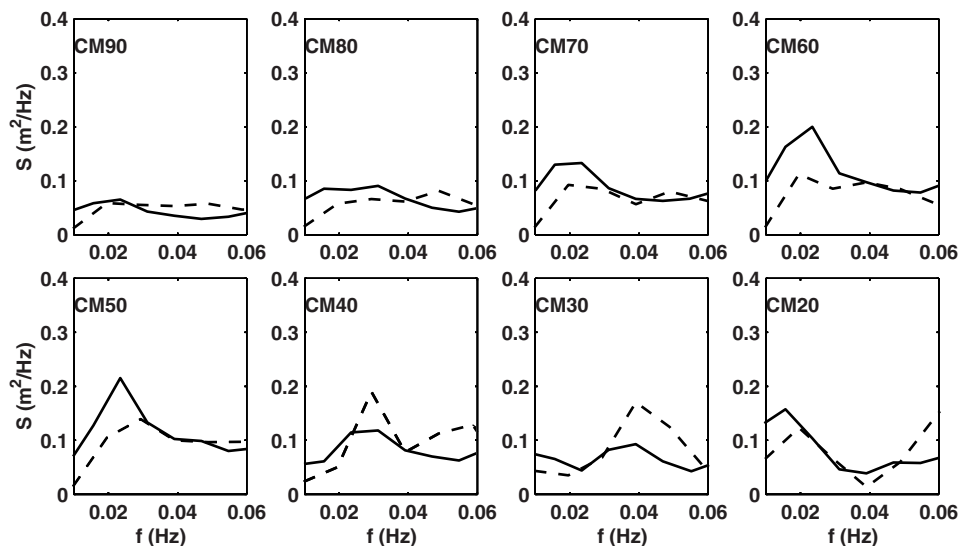


**Figure 7.** Computed (dashed line) and measured (solid line) infragravity surface elevation spectra going from offshore (upper left panel) toward the shoreline (lower right panel) on 10 October for hour 7.

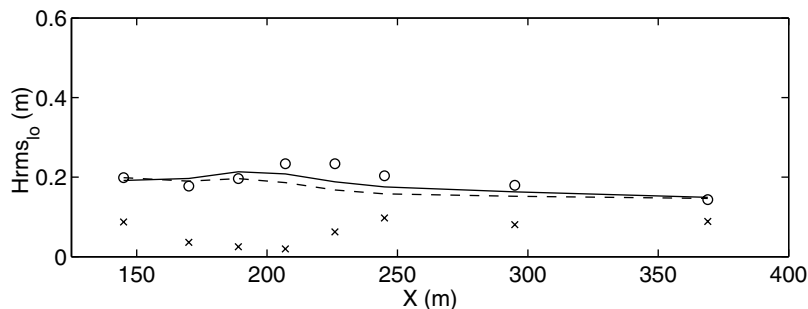


**Figure 8.** Computed (solid line) and measured (o)  $H_{rms,lo}$  on 10 October for hour 7. The theoretical depth variation for leaky waves ( $h^{-1/4}$ ) given as a reference (dashed line) calibrated with measured  $H_{rms,lo}$  at CM20 ( $X = 145$  m). Bispectrally estimated bound  $H_{rms,lo}$  denoted by (x).

when incident shortwave conditions are mild. The arrival of the first storm on 11 October is only partially mirrored in the computational results. The strong increase in the measured low-frequency energy density on 12 and 13 October (upper panel) is clearly present in the computational results (middle panel), though the computed frequency distribution is somewhat broader. The small increase in wave height at the end of 14 October (see Figure 3) results in an increase in both the measured and computed infragravity energy density. However, the more significant increase in  $H_{rms,hi}$  on 16 October, associated with the presence of local sea waves (see Figure 3), does not result in an increase in either the measured or computed low-frequency energy density. This

lack in infragravity response can be explained by the weaker nonlinear coupling for higher frequency waves (Figure C1).

[32] The frequency integrated results, i.e.,  $H_{rms,lo}$ , are shown in the lower panel of Figure 9. For most of the time the model results follow the measurements, with the exception of the storm on 11 October during which  $H_{rms,lo}$  is underestimated (up to 20%). The computations do show a strong increase in the  $H_{rms,lo}$  during the more severe storm on 13 October. Neither measurements nor computations show a clear tidal signature during this storm period. This lack of tidal signature for the measured infragravity waves was observed earlier by *Lippmann et al.* [1998]. The predicted bound infragravity wave heights compare reason-

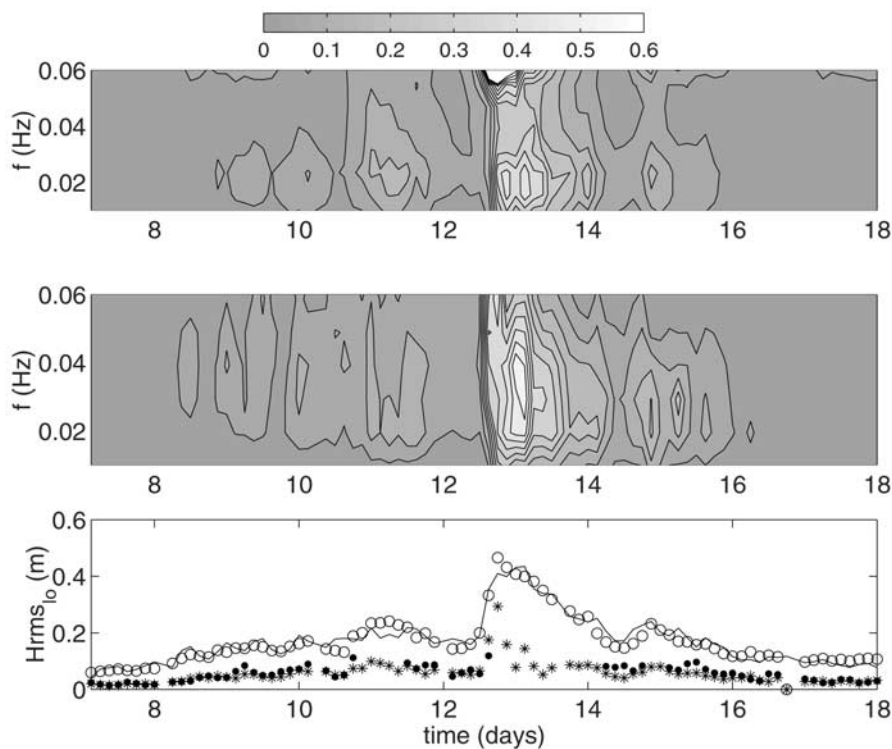


**Figure 9.** Upper panel: Synoptic view of measured surface elevation spectral densities (in  $m^2/Hz$ ) at CM90 (offshore) from 7 to 17 October. Middle panel: Similar for computed results. Lower panel: Corresponding measured (o) and computed (solid line) total  $H_{rms,lo}$  and measured (\*) and computed (dots) bound  $H_{rms,lo}$  (only shown during occasions in which the  $H_{rms,hi}$  over water depth ratio is less than 0.2).

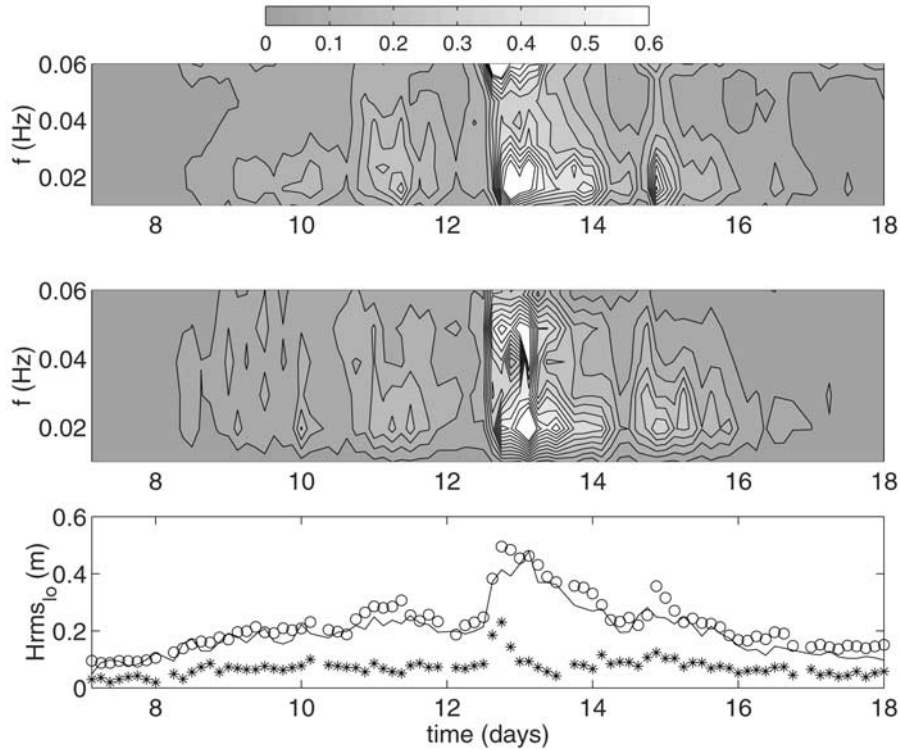


**Figure 10.** Upper panel: Synoptic view of measured surface elevation spectral densities (in  $\text{m}^2/\text{Hz}$ ) at CM70 (outer surfzone) from 7 to 17 October. Middle panel: Similar for computed results. Lower panel: Corresponding measured (o) and computed (solid line) total  $H_{rms,lo}$  and measured (\*) bound  $H_{rms,lo}$ .

ably well with the bispectral analysis of the measurements provided the wave height over water depth ratio stays below 0.2. The measured bound infragravity wave height increases for higher swell conditions, but still is always considerably less than the total infragravity wave height, explaining typically 10–15% of the infragravity energy present (i.e., 30–40% of the infragravity wave height) at this location.

[33] At the seaward side of the bar crest (at CM70), the measured frequency distribution shows an increase in the overall level of the energy density compared to CM90, which is mostly matched by the computations (upper and middle panel of Figure 10). Both measurements and computations show more structure in the frequency distribution with a peak in energy density at 0.02 Hz. The strong increase in the observed energy density during the event on 13 October is present in the computational results, but again less so at 11 October. The infragravity energy density during storm conditions is typically underestimated. This is more apparent in the comparison of the infragravity wave height (lower panel of Figure 10), in which the measurements are underestimated ( $O(20\%)$ ) by the computational results during the various storm events. On average, the bound infragravity waves have increased in height compared to CM90, though their relative contribution to the total infragravity wave height stays approximately the same. This is contrary to the expected behavior that the bound infragravity waves should increase their relative contribution as the shortwave height over depth ratio becomes larger [Elgar *et al.*, 1992; Herbers *et al.*, 1994], provided wave breaking is not important [Ruessink, 1998]. The present result is most likely related to the contribution of trapped waves, which are

dominant close to the shore line but less so at the intermediate depths (8–13 m) considered in those studies.

[34] In the vicinity of the bar crest (at CM40), the frequency distribution of the energy density exhibits a clear nodal structure (upper and middle panel of Figure 11). Horizontal ridges of measured and computed energy density coincide, with relatively high energy density levels around 0.03 Hz. The arrivals of the individual storms on the 11, 13, and 15 October are mirrored in the computational results. Contrary to CM70 the overall energy density levels during these storms are being overestimated, which is confirmed by the frequency integrated results shown in the lower panel of Figure 11. The relative contribution of the bound infragravity waves to the total infragravity wave height is smaller than at the previous locations, with the exception at the beginning of the storm on 13 October, which shows a maximum in the bound infragravity wave height.

[35] In the trough (at CM20), the nodal structure is even more prominent, given the fact that the position is closer to the shore line, and therefore, frequency and directional dispersion is limited (upper and middle panel of Figure 12). Two distinct bands of high infragravity energy density are present at 0.01 and 0.05 Hz, respectively, in both measurements and computations. The computations show a more pronounced tidal influence at this location, which is not always as strong in the measurements, except for the calm days at the beginning of the experiment. This is more evident in the frequency integrated results (lower panel of Figure 12), where both measured and computed  $H_{rms,lo}$  display a tidal variation up to 10 October. This tidal signature mostly disappears in the measured signal after

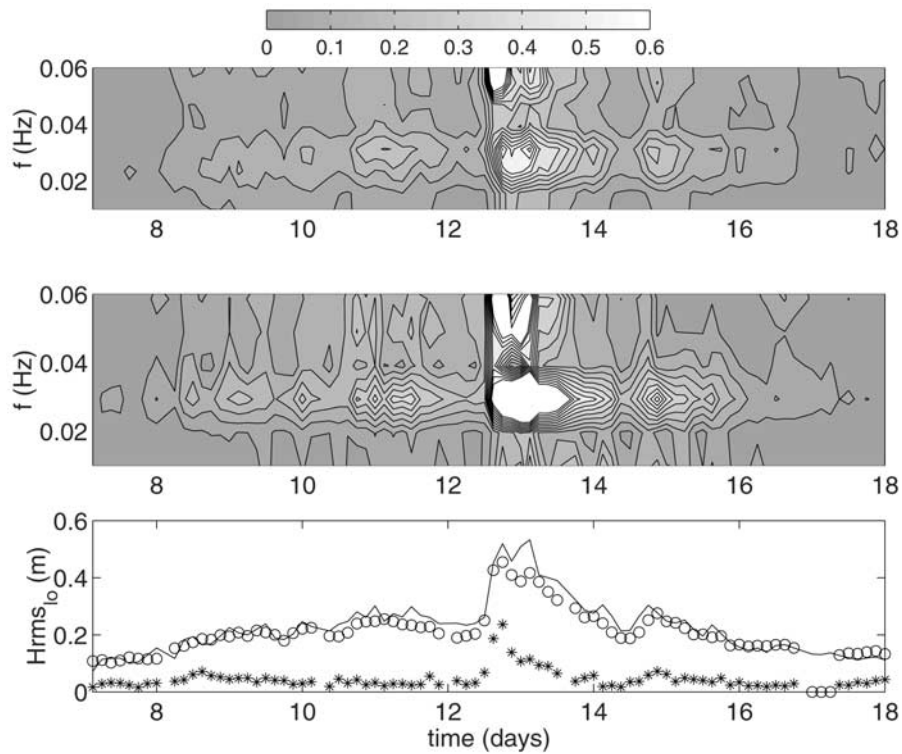


**Figure 11.** Upper panel: Synoptic view of measured surface elevation spectral densities (in  $\text{m}^2/\text{Hz}$ ) at CM40 (inner surfzone) from 7 to 17 October. Middle panel: Similar for computed results. Lower panel: Corresponding measured (o) and computed (solid line) total  $H_{rms,lo}$  and measured (\*) bound  $H_{rms,lo}$ .

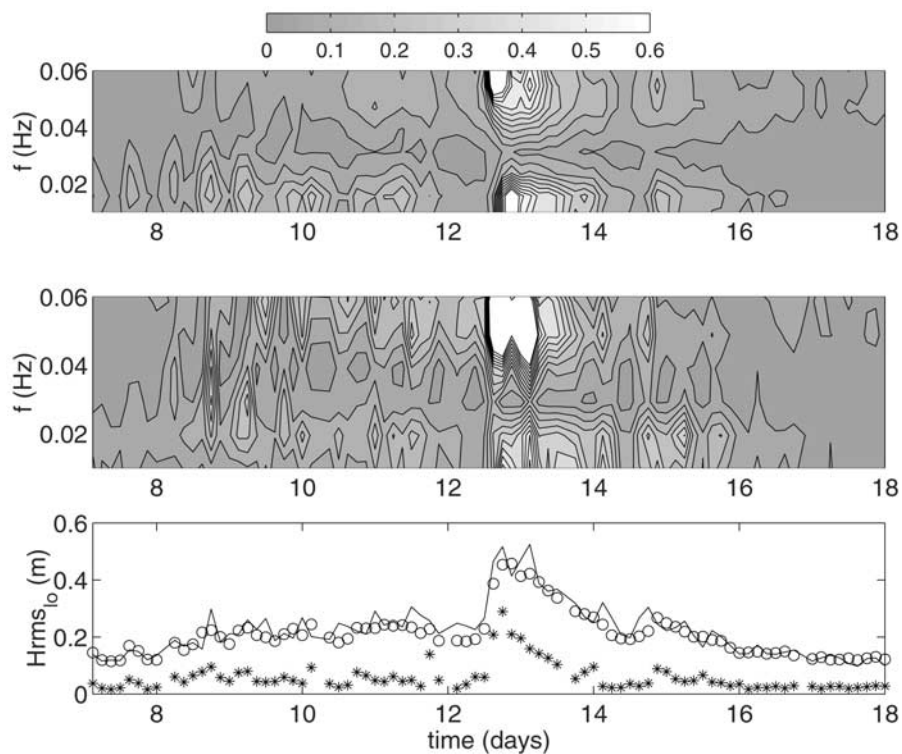


**Figure 12.** Upper panel: Synoptic view of measured surface elevation spectral densities (in  $\text{m}^2/\text{Hz}$ ) at CM20 (trough region) from 7 to 17 October. Middle panel: Similar for computed results. Lower panel: Corresponding measured (o) and computed (solid line) total  $H_{rms,lo}$  and measured (\*) bound  $H_{rms,lo}$ .

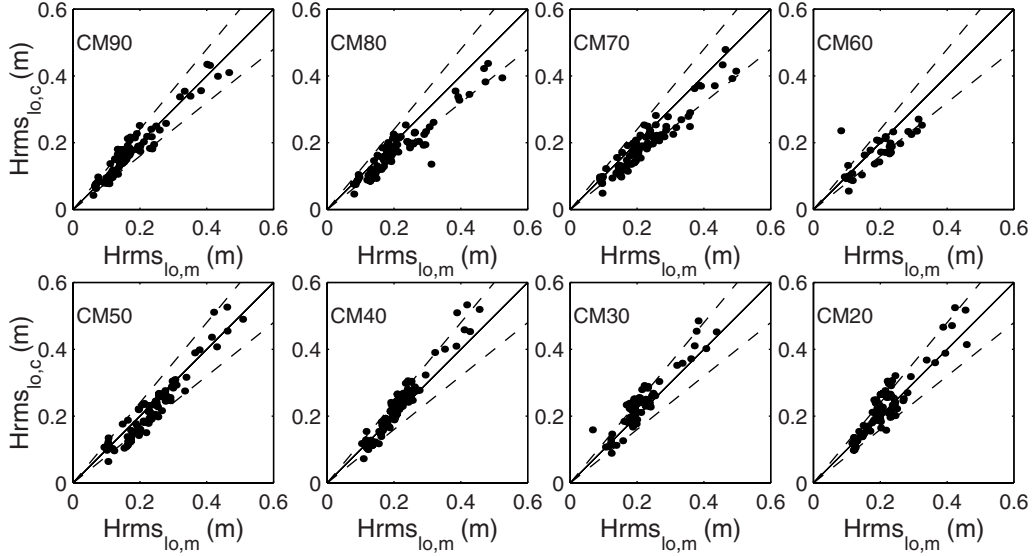


**Figure 13.** Computed (subscript c)  $H_{rms,lo}$  versus measured (subscript m)  $H_{rms,lo}$  for all days going from offshore (upper left panel) toward the shore (lower right panel). 20% error bands are indicated by the dashed lines.

10 October, whereas it persists in the computations. During the storm on 13 October, the bound infragravity wave height reaches a maximum at this location, explaining up to 50% of the total infragravity wave height present at that time.

[36] The comparison of  $H_{rms,lo}$  for all locations and times is summarized in Figure 13, plotting the predicted values versus measurements. Overall the results are within the 20% error bands indicated by the dashed lines in Figure 13. The predictive model skill is defined as [Gallagher et al., 1998]:

$$skill = 1 - \frac{\sqrt{\langle (H_{rms,lo,m} - H_{rms,lo,c})^2 \rangle}}{\sqrt{\langle (H_{rms,lo,m})^2 \rangle}} \quad (32)$$

where the subscripts  $m$  and  $c$  refer to measured and computed values respectively and  $\langle \rangle$  denotes averaging. The mean skill value is 0.83 (see Table 2), typically explaining 80% of the measured variability in  $H_{rms,lo}$  throughout the 11 day period. Differences occur mainly during storm conditions when the outer surf zone positions (CM70–CM80) are biased low and the inner surf zone positions (CM30–CM40) are biased high. For the milder conditions the results are mostly scattered around the diagonal, representing perfect agreement, though with an increased spreading for the positions closer to the shoreline (CM20–CM30). Both CM60 and CM30 have fewer points due to instrument break down during the 11 day period.

#### 4. Discussion

[37] In the infragravity computations, the presence of setup, longshore currents, roller energy and bottom friction have been taken into account. The sensitivity of the computational infragravity results to these phenomena, expressed in changes in the skill factor with respect to the default case, is summarized in Table 2. The influence of the

setup of the mean water level on the predicted  $H_{rms,lo}$  is negligible for the stations further away from the shoreline (CM90–CM50). Closer to shore (CM40–CM20) inclusion of the setup affects the prediction of  $H_{rms,lo}$  in a positive way [van Dongeren, 1997] given the presence of nodes and antinodes. The longshore current affects the predicted  $H_{rms,lo}$  predominantly within the surf zone through the bottom friction, equations (22) and (23), with the largest differences close to the maximum longshore velocity position which resided in the trough (CM30) for most of the 11 day period. Edge wave amplification over the bar with respect to its shoreline intensity [Schönfeldt, 1995; Bryan and Bowen, 1996] is not evident in the computed  $H_{rms,lo}$  if the longshore current is included and is not expected for the infragravity frequencies considered here [Bryan and Bowen, 1998]. Excluding the roller in the forcing has a more or less equal effect on all measuring points, typically resulting in a 10–15% decrease in the predicted  $H_{rms,lo}$ . Still, the qualitative impact of the roller is small, i.e., it is merely enhancing the infragravity wave height throughout the surf zone as opposed to the setup and longshore current which

**Table 2.** Skill and Skill Differences (Going From Left to Right) for the Prediction of  $H_{rms,lo}$  at the Various Measurement Positions for the Default Computation, Excluding Setup, Longshore Currents, Roller Energy, and Roller Energy in Combination With a Smaller Friction Factor ( $c_f = 0.003$ ), Respectively

Position	Skill	$\Delta$ Skill ( $-\bar{\eta}$ )	$\Delta$ Skill ( $-I$ )	$\Delta$ Skill ( $-E_r$ )	$\Delta$ Skill ( $-E_r, \Delta c_f$ )
CM90	0.87	0.00	-0.13	-0.12	-0.05
CM80	0.80	0.02	0.04	-0.17	-0.08
CM70	0.83	0.02	-0.02	-0.18	-0.08
CM60	0.77	0.02	-0.03	-0.15	-0.06
CM50	0.86	-0.01	-0.11	-0.19	-0.10
CM40	0.84	-0.05	-0.24	-0.08	0.02
CM30	0.84	-0.05	-0.24	-0.08	0.01
CM20	0.83	-0.05	-0.19	-0.12	-0.02
mean	0.83	-0.01	-0.12	-0.14	-0.05

affect the spatial structure of the infragravity field. The same holds for the bottom friction, which increases the predicted  $H_{rms,lo}$  throughout the domain for a decreased friction factor of 0.003, thus counteracting the omission of the roller effect in the infragravity computations. Still, neither the bottom friction factor ( $c_f$ ) nor the roller dissipation parameter ( $\beta$ ) are free tuning parameters for infragravity wave computations as they have a pronounced affect on the computed mean longshore current velocity distributions [RB97; Ruessink *et al.*, 2001].

[38] The computational infragravity results are generally sensitive to the dissipation formula used in the modulated wave and roller balance equations. *Symonds et al.* [1982] used a constant breaker wave height to water depth ratio to determine the wave height at a given depth in the surf zone:

$$H = \gamma h \quad (33)$$

The wave energy modulation thus results in a time varying position of the breakpoint, which acts as an infragravity wave maker. Once all the waves are breaking the modulation is destroyed and subsequently no infragravity waves are generated in the region beyond this point according to this model. *Schäffer and Svendsen* [1988] allowed the modulation to enter the inner surf zone resulting in a significant contribution to the total infragravity surface elevation in their linear model computations. A similar approach was taken by *Watson and Peregrine* [1992] who used a nonlinear model for the infragravity motions in the inner surf zone obtaining good agreement with measurements.

[39] The coefficient of variation,  $COV$ , is used as a measure for the modulation of the local wave energy on the timescale of wave groups with respect to its mean:

$$COV = \frac{\sigma_A}{\bar{A}} \quad (34)$$

where  $\sigma_A$  and  $\bar{A}$  are respectively the standard deviation and the mean of the slowly varying shortwave envelope. The measurements show that the modulation (Figure 14) decays slightly as the shortwaves break on the seaward side of the bar (around  $X = 225$  m, see also Figure 4), but mostly persists throughout the surf zone (similar observations were made by *List* [1991]). The slight decay of the modulation over the bar indicates that the breakpoint variation is present, though its contribution to the infragravity forcing is expected to be small in line with the analysis by *List* [1992]. This is typical for the 11 days considered here, thus supporting the use of the dissipation formulation by *Eldeberky and Battjes* [1996] that sustains the modulation throughout the surf zone. Ignoring the breakpoint variation is expected to result in a slight overestimation of the infragravity forcing in the inner surf zone and an underestimation of the forcing around the breakpoint, thus contributing to the observed bias in the predicted infragravity wave heights (see Figure 13).

## 5. Conclusions

[40] A linear model has been developed to examine the generation of infragravity waves forced by directionally

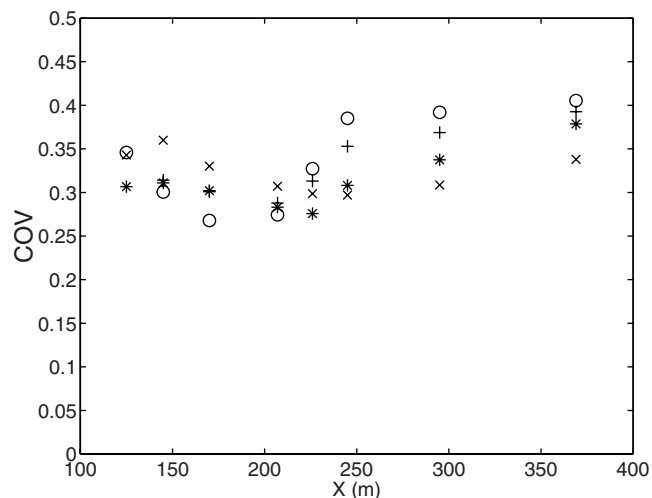


**Figure 14.** Cross-shore variation of the energy modulation for 10 October at high tide (o) and low tide (+). Similar for 13 October at high tide (\*) and low tide (x).

spread shortwaves incident on an alongshore uniform beach with an arbitrary cross-shore bottom profile. Integrating the computed infragravity spectra over all directional contributions results in the frequency distribution of the surface elevation infragravity spectra. These have been compared with measured spectra obtained during the Delilah field experiment. In general the computed frequency distributions mimic the observations with relatively broad infragravity spectra offshore of the bar crest and a clear nodal structure closer to the shore. The strong increases in infragravity energy density associated with the arrival of individual storms are predicted throughout the surf zone with the exception of the storm on 11 October.

[41] The comparisons between measured and computed  $H_{rms,lo}$  show that the computations explain typically 80% of the measured infragravity wave height variability present in the surf zone. The sensitivity analysis indicates the importance of including rollers, longshore current velocity profiles and setup, where the latter two affect the cross-shore structure of the infragravity wave field. Omission of the roller energy balance can be counteracted by utilizing a smaller bottom friction coefficient. However, both roller energy and bottom friction are important in the prediction of the mean longshore current velocity profile and cannot be changed at will.

[42] The contribution of the bound infragravity waves to the total infragravity wave height is shown to be typically in the order of 30% throughout the 11 day period, though this can increase to approximately 50% during energetic storm events (Figure 12). Comparison of the predicted bound infragravity energy at approximately 4 m water depth (CM90) compares well with the results from the bispectral analysis provided the root mean square wave height over water depth ratio stays below 0.2.

## Appendix A. Including a Longshore Current

[43] Linearizing the shallow water equations as given by *Phillips* [1977], including a steady alongshore uniform

longshore current following *Howd et al.* [1992], the continuity equation is given by:

$$\frac{\partial \eta}{\partial t} + \frac{\partial(hu)}{\partial x} + \frac{\partial(hv)}{\partial y} + \frac{\partial \eta V}{\partial y} = 0 \quad (\text{A1})$$

with the cross-shore momentum equation given by:

$$\frac{\partial u}{\partial t} + V \frac{\partial u}{\partial y} + g \frac{\partial \eta}{\partial x} = -F^x \quad (\text{A2})$$

and the alongshore momentum equation:

$$\frac{\partial v}{\partial t} + u \frac{dV}{dx} + V \frac{\partial v}{\partial y} + g \frac{\partial \eta}{\partial y} = -F^y \quad (\text{A3})$$

where the forcing terms are given by:

$$F^x = \frac{1}{\rho h} \left( \frac{\partial S_{xx}}{\partial x} - \frac{\partial S_{xy}}{\partial y} \right) \quad (\text{A4})$$

and:

$$F^y = \frac{1}{\rho h} \left( \frac{\partial S_{yy}}{\partial y} - \frac{\partial S_{yx}}{\partial x} \right) \quad (\text{A5})$$

and the superscript denotes the direction in which they operate. Using infragravity wave solutions that are periodic in both time and alongshore direction, e.g., equation (15), for  $\eta$ ,  $u$ ,  $v$  and  $F^i$  and introducing these in equations (A1)–(A3) gives (dropping periodicity):

$$\hat{\eta} = \frac{-\frac{d\hat{u}}{dx} + i\Delta k_y h \hat{v}}{(i\Delta\omega - i\Delta k_y V)} \quad (\text{A6})$$

$$\hat{u} = \frac{-g \frac{d\hat{\eta}}{dx} - \hat{F}^x}{(i\Delta\omega - i\Delta k_y V)} \quad (\text{A7})$$

$$\hat{v} = \frac{ig\Delta k_y \hat{\eta} - \frac{d\hat{v}}{dx} \hat{u} - \hat{F}^y}{(i\Delta\omega - i\Delta k_y V)} \quad (\text{A8})$$

Combining equations (A6)–(A8) to eliminate both  $\hat{u}$  and  $\hat{v}$  gives:

$$\begin{aligned} & -\frac{d}{dx} \left[ \frac{gh \frac{d\hat{\eta}}{dx}}{(i\Delta\omega - i\Delta k_y V)^2} \right] + \hat{\eta} \left[ 1 + \frac{gh\Delta k_y^2}{(i\Delta\omega - i\Delta k_y V)^2} \right] \\ & = -\frac{d}{dx} \left[ \frac{hF^x}{(i\Delta\omega - i\Delta k_y V)^2} \right] + \left[ \frac{i\Delta k_y h F^y}{(i\Delta\omega - i\Delta k_y V)^2} \right] \end{aligned} \quad (\text{A9})$$

which, on substitution of the effective depth, equation (24), gives:

$$\begin{aligned} & h' \frac{d^2 \hat{\eta}}{dx^2} + \frac{dh'}{dx} \frac{d\hat{\eta}}{dx} + \left( \frac{4\pi^2 \Delta f^2}{g} - \frac{i\mu 2\pi \Delta f}{g} - h' \Delta k_y^2 \right) \hat{\eta} \\ & = \frac{1}{g} \left( \frac{d}{dx} [h' F^x] - i\Delta k_y h' F^y \right) \end{aligned} \quad (\text{A10})$$

to which the linear damping term has been added. This equation is similar to equation (16) with a small modification of the RHS to account for the presence of the effective depth in the forcing. Without the longshore current, i.e.,  $h' = h$ , equation (16) is retrieved.

## Appendix B. Boundary Conditions

[44] The offshore wave boundary is composed of a bound incoming infragravity wave and a free outgoing infragravity wave, described by the following characteristic equations:

$$\frac{\partial \eta_b}{\partial t} + \frac{2\pi \Delta f}{\Delta k} \cos \hat{\theta}_{in} \frac{\partial \eta_b}{\partial x} + \frac{2\pi \Delta f}{\Delta k} \sin \hat{\theta}_{in} \frac{\partial \eta_b}{\partial y} = 0 \quad (\text{B1})$$

$$\frac{\partial \eta_{out}}{\partial t} - \sqrt{gh} \cos \hat{\theta}_{out} \frac{\partial \eta_{out}}{\partial x} - \sqrt{gh} \sin \hat{\theta}_{out} \frac{\partial \eta_{out}}{\partial y} = 0 \quad (\text{B2})$$

where  $\eta_{out}$  represents the free outgoing infragravity wave and  $\eta_b$  the bound incoming infragravity wave forced by two shortwave spectral components. Combining these equations to obtain an expression for the total surface elevation at the offshore boundary gives:

$$\begin{aligned} & \frac{\partial \eta}{\partial t} - \sqrt{gh} \cos \hat{\theta}_{out} \frac{\partial \eta}{\partial x} - \sqrt{gh} \sin \hat{\theta}_{out} \frac{\partial \eta}{\partial y} \\ & = \left( \sqrt{gh_0} \cos \hat{\theta}_{out} + \frac{2\pi \Delta f}{\Delta k} \cos \hat{\theta}_{in} \right) \frac{\partial \eta_b}{\partial x} \\ & + \left( \sqrt{gh_0} \sin \hat{\theta}_{out} + \frac{2\pi \Delta f}{\Delta k} \sin \hat{\theta}_{in} \right) \frac{\partial \eta_b}{\partial y} \end{aligned} \quad (\text{B3})$$

where the exit angle of the free infragravity wave is obtained from Snell's law:

$$\hat{\theta}_{out} = -\text{asin} \left( \frac{\Delta k_y \sqrt{gh_0}}{2\pi \Delta f} \right) \quad (\text{B4})$$

with  $h_0$  the water depth at the offshore boundary. The incidence angle of the bound infragravity wave is known through equation (29). Once the bound infragravity wave is computed from the local forcing at the offshore boundary (see Appendix C), the boundary condition is determined.

[45] At the shore line the infragravity waves are assumed to reflect, giving the following condition for the surface elevation at the shore line:

$$\frac{\partial \eta}{\partial x} = \frac{-1}{\rho gh} \left( \frac{\partial S_{xx}}{\partial x} + \frac{\partial S_{xy}}{\partial y} \right) \quad (\text{B5})$$

which was obtained from the cross-shore momentum balance, equation (2), by setting the cross-shore velocity to zero (in line with perfect reflection). The condition is applied at a depth of 0.1 m to avoid singularities given the presence of finite forcing.

[46] The analytical solution given by *Schäffer* [1993, 1994] was used to verify the numerics, considering coincident shortwaves with an incidence angle of 30°, a mean frequency of 1 Hz on a plane sloping beach of 1:20

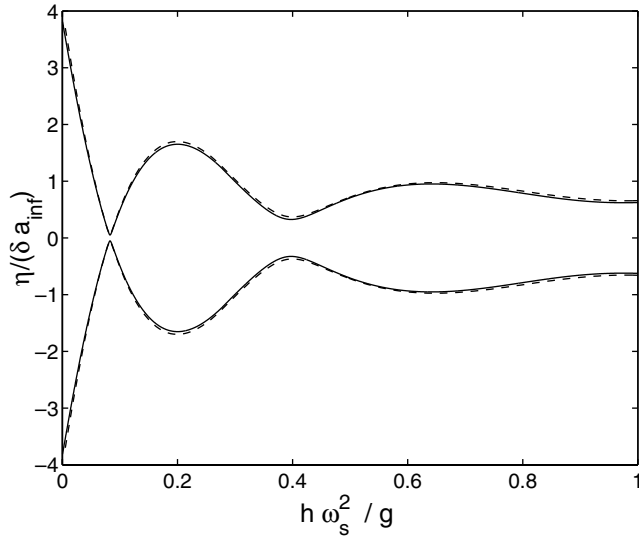


**Figure B1.** Comparison of computational infragravity surface elevation envelope (solid line) with analytical solution by Schäffer [1993] (dashed line).

preceded by a horizontal shelf with a water depth of 0.254 m. The amplitude modulation,  $\delta$  is 0.1 with a difference frequency of 0.02 Hz. The infragravity surface elevation envelope is compared with the analytical solution in Figure B1, showing a good match.

### Appendix C. Bound Infragravity Energy

[47] A general expression to compute the infragravity energy forced by a directional shortwave spectrum on an arbitrary depth was given by Hasselmann [1962]. Instead of using this, an expression is derived which is consistent with the radiation stress approach used in the present linear model. Assuming a steady state on a horizontal bed, the bound infragravity wave amplitude, denoted  $\hat{\eta}_b$ , can be obtained from equation (4), substituting expressions (5) to (15) which are now also periodic in  $x$ :

$$\begin{aligned} & \rho g \left( \frac{4\pi^2 \Delta f^2 \hat{\eta}_b}{g} - \Delta k_x^2 h \hat{\eta}_b - \Delta k_y^2 h \hat{\eta}_b - \frac{i\mu 2\pi \Delta f \hat{\eta}_b}{g} \right) \\ & \cdot \exp[i(2\pi \Delta f t - \Delta k_y y - \Delta k_x x)] + * = \left( \Delta k_x^2 [n(1 + \cos^2 \hat{\alpha}) - 0.5] \right. \\ & \left. + 2i \Delta k_y \Delta k_x (n \cos \hat{\alpha} \sin \hat{\alpha}) + \Delta k_y^2 [n(1 + \sin^2 \hat{\alpha}) - 0.5] \right) \\ & \cdot \hat{E}_w \exp[i(2\pi \Delta f t - \Delta k_y y - \Delta k_x x)] + * \end{aligned} \quad (C1)$$

Dividing by the squared infragravity wave number,  $(\Delta k)^2$ , and using the identities:

$$\frac{\Delta k_x^2}{\Delta k^2} = \cos^2(\hat{\theta}_m)$$

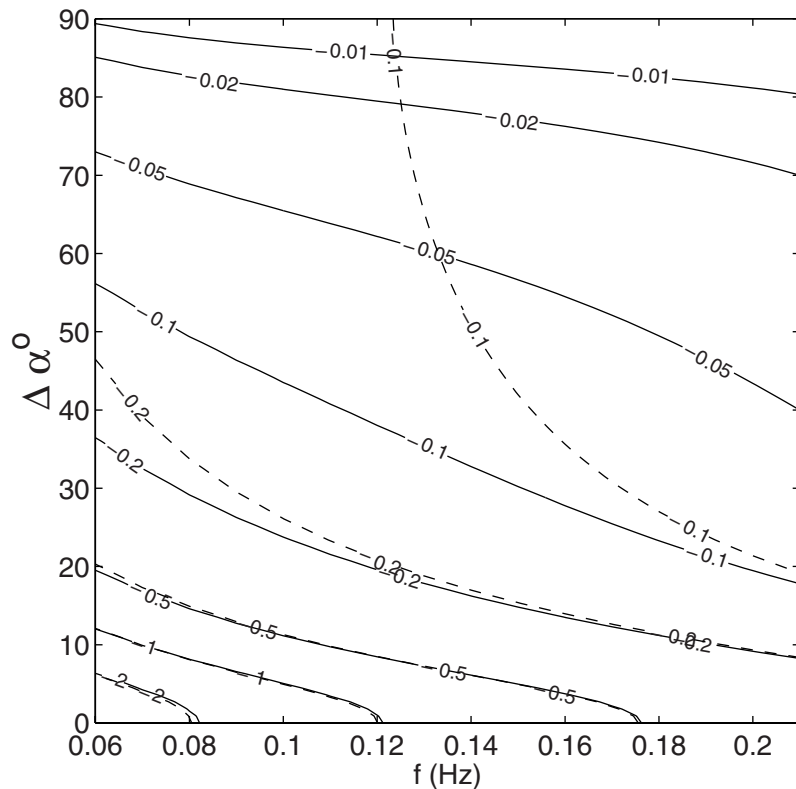


**Figure C1.** Comparison of difference interaction coefficient equation (C6) (dashed line) for  $\Delta f = 0.03$  Hz at 4.5 m water depth with nonlinear coupling coefficient (solid line) given by Hasselmann [1962].

$$\frac{\Delta k_x \Delta k_y}{\Delta k^2} = \cos(\hat{\theta}_{in}) \sin(\hat{\theta}_{in}) \quad (C2)$$

$$\frac{\Delta k_y^2}{\Delta k^2} = \sin^2(\hat{\theta}_{in})$$

where the incidence angle of the bound infragravity wave,  $\hat{\theta}_{in}$ , is obtained from equation (29), an expression for the bound infragravity wave amplitude on a horizontal plane is found as:

$$\hat{\eta}_b = \frac{\left( n \left( 1 + \cos^2(\hat{\alpha} - \hat{\theta}_{in}) \right) - \frac{1}{2} \right) \hat{E}}{\rho \left( \frac{4\pi^2 \Delta f^2}{\Delta k^2} - \frac{i\mu 2\pi \Delta f}{\Delta k^2} - gh \right)} \quad (C3)$$

For the case of two shortwave components from the same direction and neglecting bottom friction, the solution of *Longuet-Higgins and Stewart* [1962] is recovered:

$$\hat{\eta}_b = \frac{(2n - \frac{1}{2}) \hat{E}}{\rho \left( \frac{4\pi^2 \Delta f^2}{\Delta k^2} - gh \right)} \quad (C4)$$

[48] The bound energy density,  $S_b$ , for a specific  $\Delta f$  is obtained by transforming the amplitude equation (C3) to spectral densities and integrating all directional contributions:

$$S_b(\Delta f) = 2 \int_{f_{c,lo}}^{\infty} \int_{-\frac{\pi}{2}}^{\frac{\pi}{2}} \int_{-\frac{\pi}{2}}^{\frac{\pi}{2}} |C|^2 S(f + \Delta f, \alpha_1) S(f, \alpha_2) df d\alpha_1 d\alpha_2 \quad (C5)$$

where the difference interaction coefficient  $C$  is given by:

$$C(f + \Delta f, f, \alpha_1, \alpha_2) = \frac{g \left( n \left( 1 + \cos^2(\hat{\alpha} - \hat{\theta}_{in}) \right) - \frac{1}{2} \right)}{\left( \frac{4\pi^2 \Delta f^2}{\Delta k^2} - \frac{i\mu 2\pi \Delta f}{\Delta k^2} - gh \right)} \quad (C6)$$

The difference interaction coefficient (neglecting friction) is compared to the nonlinear solution by *Hasselmann* [1962] in Figure C1. A good match is obtained for difference angles between the shortwave components up to 30°. For larger difference angles, the present formulation overpredicts the coupling coefficient. However, in this region the nonlinear coupling between the two primary waves and the long wave ( $2|C|^2$ ) drops off quickly and the resulting errors in the bound infragravity energy density are expected to be small.

[49] **Acknowledgments.** This work results from a collaboration with the Naval Postgraduate School, which enabled us to use the time series obtained during the Delilah field experiment. Additional data were provided by the Field Research Facility of the U.S. Army Engineer Waterways Experiment Station's Coastal Engineering Research Center. Permission to use these data is appreciated. The sponsoring by the National Institute for Coastal and Marine Management (RIKZ) through the Netherlands Center for Coastal Research (NCK) to perform this work is greatly appreciated. Additional funding was obtained from the European Community through the project on Surf and Swash Zone Mechanics (SASME) under contract number MAS-CT97-0081. Part of this work was performed while Ad Reniers held a National Research Council Research Associateship at the Naval Postgraduate School. Ed Thornton was funded by the Office of Naval Research, Coastal Sciences Programs, under contract N00014-01-WR20023. The computational results improved substantially from discussions with Dano Roelvink on the modeling of infragravity waves. The

discussions with Tom Herbers and Mark Orzech on the bispectral analysis are much appreciated. Finally, we thank the reviewers for their constructive comments resulting in an improved paper.

## References

- Birkemeier, W. A., C. Donoghue, C. E. Long, K. H. Hathaway, and C. F. Baron, 1990 DELILAH nearshore experiment: Summary report, *Technical report CHL-97-4-24*, Field Res. Facil., U. S. Army Eng. Waterw. Exp. Stn., Vicksburg, Miss., 1997.
- Biesel, F., Equations generales au second ordre de la houle irreguliere, *Houille Blanche*, 7, 372–376, 1952.
- Bryan, K. R., and A. J. Bowen, Edge wave trapping and amplification on barred beaches, *J. Geophys. Res.*, 101, 6543–6552, 1996.
- Bryan, K. R., and A. J. Bowen, Bar-trapped edge waves and longshore currents, *J. Geophys. Res.*, 103, 27,867–27,884, 1998.
- Bowen, A. J., and D. I. Inman, Edge waves and crescentic bars, *J. Geophys. Res.*, 76, 8662–8671, 1971.
- Church, C. C., and E. B. Thornton, Effects of breaking wave induced turbulence within a longshore current model, *J. Coastal Eng.*, 20, 1–28, 1993.
- Eckart, C., Surface waves on water of variable depth, *Wave Rep. 100*, Scripps Inst. of Oceanogr., Univ. of Calif., La Jolla, 1951.
- Eldeberky, Y., and J. A. Battjes, Spectral modelling of wave breaking: Application to Boussinesq equations, *J. Geophys. Res.*, 101, 1253–1264, 1996.
- Elgar, S., T. H. C. Herbers, M. Okiihiro, J. Oltman-Shay, and R. T. Guza, Observations of infragravity waves, *J. Geophys. Res.*, 97, 15,537–15,577, 1992.
- Foda, M. A., and C. C. Mei, Nonlinear excitation of long trapped waves by a group of short swells, *J. Fluid Mech.*, 111, 319–345, 1981.
- Gallagher, B., Generation of surfbeat by non-linear wave interactions, *J. Fluid Mech.*, 49, 1–20, 1971.
- Gallagher, E. L., S. Elgar, and R. T. Guza, Observations of sand bar evolution on a natural beach, *J. Geophys. Res.*, 103, 3203–3215, 1998.
- Hasselmann, K., On the non-linear energy transfer in a gravity-wave spectrum, part I, General theory, *J. Fluid Mech.*, 12, 481–500, 1962.
- Hasselmann, K., W. Munk, and G. MacDonald, Bispectra of ocean waves, in *Time Series Analysis*, edited by M. Rosenblatt, pp. 125–139, Wiley, New York, 1963.
- Herbers, T. H. C., Steve Elgar, and R. T. Guza, Infragravity-frequency (0.005–0.05 Hz) motions on the shelf, part I, Forced waves, *J. Phys. Oceanogr.*, 24, 917–927, 1994.
- Herbers, T. H. C., Steve Elgar, R. T. Guza, and W. C. O'Reilly, Infragravity-frequency (0.005–0.05 Hz) motions on the shelf, part II, Free waves, *J. Phys. Oceanogr.*, 25, 1063–1079, 1995a.
- Herbers, T. H. C., Steve Elgar, and R. T. Guza, Generation and propagation of infragravity waves, *J. Geophys. Res.*, 100, 24,863–24,872, 1995b.
- Holman, R. A., Infragravity energy in the surf zone, *J. Geophys. Res.*, 86, 6442–6450, 1981.
- Holman, R. A., and A. J. Bowen, Bars, bumps and holes: Models for the generation of complex beach topography, *J. Geophys. Res.*, 87, 457–468, 1982.
- Howd, P. J., A. J. Bowen, and R. A. Holman, Edge waves in the presence of strong longshore currents, *J. Geophys. Res.*, 97, 11,357–11,371, 1992.
- Huntley, D. A., Long period waves on a natural beach, *J. Geophys. Res.*, 81, 871–885, 1976.
- Huntley, D. A., R. T. Guza, and E. B. Thornton, Field observations of surf beats, I, Progressive edge waves, *J. Geophys. Res.*, 86, 6451–6466, 1981.
- List, J. H., Wave groupiness variations in the nearshore, *J. Coastal Eng.*, 15, 475–496, 1991.
- List, J. H., A model for two-dimensional surfbeat, *J. Geophys. Res.*, 97, 5623–5635, 1992.
- Lippmann, T. C., R. A. Holman, and A. J. Bowen, Generation of edge waves in shallow water, *J. Geophys. Res.*, 102, 8663–8679, 1997.
- Lippmann, T. C., T. H. C. Herbers, and E. B. Thornton, Gravity and shear wave contributions to nearshore infragravity motions, *J. Phys. Oceanogr.*, 24, 231–239, 1998.
- Long, C. E., and J. Atmadja, Index and bulk parameters for frequency-directional spectra measured at CERC Field Research Facility, September 1990 to August 1991, *Miscellaneous paper CERC-94-5*, U.S. Army Waterw. Exp. Stn., Vicksburg, Miss., 1994.
- Longuet-Higgins, M. S., and R. W. Stewart, Radiation stress and mass transport in surface gravity waves with application to “surf beats”, *J. Fluid Mech.*, 29, 481–504, 1962.
- Longuet-Higgins, M. S., and R. W. Stewart, Radiation stresses in water waves: A physical discussion, with applications, *Deep Sea Res.*, 11, 529–562, 1964.
- Mei, C. C., and C. Benmoussa, Long waves induced by short wave groups over an uneven bottom, *J. Fluid Mech.*, 139, 219–235, 1984.

- Munk, W. H., Surf beats, *Eos Trans. AGU*, 30, 849–854, 1949.
- Naim, R. B., J. A. Roelvink, and H. N. Southgate, Transition zone width and implications for modelling surfzone hydrodynamics, in *Proc. 22nd Int. Conf. Coastal Eng., New York*, pp. 68–81, Am. Soc. of Civ. Eng., New York, 1990.
- Okiihiro, M., R. T. Guza, and R. J. Seymour, Bound infragravity waves, *J. Geophys. Res.*, 97, 11,453–11,469, 1992.
- Phillips, O. M., *The Dynamics of the Upper Ocean*, 2nd ed., 336 pp., Cambridge Univ. Press, New York, 1977.
- Reniers, A. J. H. M., and J. A. Battjes, A laboratory study of longshore currents over barred and non-barred beaches, *J. Coastal Eng.*, 30, 1–22, 1997.
- Roelvink, J. A., Surf beat and its effect on cross-shore profiles, PhD thesis, Delft Univ. of Technol., Netherlands, 1993.
- Roelvink, J. A., and M. J. F. Stive, Bar generating cross-shore flow mechanisms on a beach, *J. Geophys. Res.*, 94, 4785–4800, 1989.
- Ruessink, B. G., Bound and free infragravity waves in the nearshore zone under breaking and nonbreaking conditions, *J. Geophys. Res.*, 103, 12,795–12,805, 1998.
- Ruessink, B. G., J. R. Miles, F. Feddersen, R. T. Guza, and S. Elgar, Modeling the alongshore current on barred beaches, *J. Geophys. Res.*, 106, 22,451–22,463, 2001.
- Schäffer, H. A., Infragravity waves induced by short-wave groups, *J. Fluid Mech.*, 247, 551–588, 1993.
- Schäffer, H. A., Edge waves forced by short-wave groups, *J. Fluid Mech.*, 259, 125–148, 1994.
- Schäffer, H. A., and L. A. Svendsen, Surf beat generation on a mild-slope, in *Proc. 21st Int. Conf. Coastal Eng. Malaga*, pp. 1058–1072, Am. Soc. of Civ. Eng., New York, 1988.
- Schönfeldt, H. J., On the modification of edge waves by longshore currents, *Cont. Shelf Res.*, 15, 1213–1221, 1995.
- Suhayda, J. N., Standing waves on beaches, *J. Geophys. Res.*, 79, 3065–3071, 1974.
- Symonds, G., D. A. Huntley, and A. J. Bowen, Two-dimensional surfbeat: Long wave generation by a time varying breakpoint, *J. Geophys. Res.*, 87, 492–498, 1982.
- Stive, M. J. F., and H. J. de Vriend, Shear stresses and mean flow in shoaling and breaking waves, in *Proc. 24th Int. Conf. Coastal Eng., Kobe*, pp. 594–608, Am. Soc. of Civ. Eng., New York, 1994.
- Thornton, E. B., and R. T. Guza, Energy saturation and phase speeds measured on a natural beach, *J. Geophys. Res.*, 87, 9499–9508, 1982.
- Thornton, E. B., and C. S. Kim, Longshore current and wave height modulation at tidal frequency inside the surfzone, *J. Geophys. Res.*, 98, 16,509–16,519, 1993.
- Tucker, M. J., Surfbeats: Sea waves of 1 to 5 minutes' period, *Proc. R. Soc. London, Ser. A*, 202, 565–573, 1950.
- van Dongeren, A. R., Numerical modelling of quasi-3d nearshore hydrodynamics, PhD thesis, University of Delaware, USA, 1997.
- Van Leeuwen, P. J., Low frequency wave generation due to breaking wind waves, PhD thesis, Delft Univ. of Technol., Netherlands, 1992.
- Watson, G., and D. H. Peregrine, Low frequency waves in the surfzone, in *Proc. 23rd Int. Conf. Coastal Eng., Venice, Italy*, pp. 818–831, Am. Soc. of Civ. Eng., New York, 1992.

---

A. J. H. M. Reniers and E. B. Thornton, Oceanography Department, Naval Postgraduate School, Spanagel Hall, Monterey, CA 93943, USA. (reniers@oc.nps.navy.mil)

J. A. Battjes and A. R. van Dongeren, Dutch Center for Coastal Research (NCK), Faculty of Civil Engineering and Geosciences, Delft University of Technology, Delft, Netherlands.